

## N<sub>2</sub> Physisorption on Carbon Nanotubes: Computer Simulation and Experimental Results

Juan I. Paredes, Fabián Suárez-García, Silvia Villar-Rodil, Amelia Martínez-Alonso, and Juan M. D. Tascón

*Instituto Nacional del Carbón, CSIC, Apartado 73, 33080 Oviedo, Spain*

Eduardo J. Bottani\*

*Instituto de Investigaciones Fisicoquímicas Teóricas y Aplicadas, (UNLP-CIC-CONICET), Casilla de Correo 16, Sucursal 4, (1900) La Plata, Argentina*

*Received: August 1, 2002; In Final Form: May 28, 2003*

Nitrogen physical adsorption on carbon nanotubes bundles is studied with grand canonical ensemble Monte Carlo computer simulations in a wide temperature range. The results are compared with experimental data obtained in our laboratory and with that published in the literature. The characteristics of the sample employed in this work are also presented. The nanotubes are modeled by grouping them in bundles forming a hexagonal array. Local adsorption isotherms are calculated. The adsorption potential is analyzed, and the results are employed to interpret several distributions obtained from the simulations. The location of the expected adsorption sites is confirmed. The adsorbed phase within the tubes is characterized.

### Introduction

In 1991, Iijima<sup>1</sup> announced the discovery of multiwalled carbon nanotubes as a byproduct in fullerene production. Since then, great efforts were made to improve the yield during the preparation and purification.<sup>2–8</sup> Single-walled carbon nanotubes (SWNT) are available since 1992 in enough quantities to be studied<sup>9,10</sup> and immediately attracted attention because of potential technological applications<sup>11–16</sup> and also from a basic research perspective because it was the first form of carbon that could provide physical realizations of ideal systems.<sup>17,18</sup>

Single-walled carbon nanotubes could be considered as the result of bisecting a C<sub>60</sub> molecule at the equator and the two resulting hemispheres are joined with a cylindrical tube one monolayer thick and with the same diameter as C<sub>60</sub>. If the C<sub>60</sub> molecule is bisected normal to a 5-fold axis, an armchair tubule is obtained, whereas if the bisection is made normal to a 3-fold axis, a zigzag type tubule is obtained. Other chiral tubules can be formed with a screw axis along the axis of the tubule. Carbon nanotubes can be specified in terms of the tubule diameter  $d_t$ , and chiral angle  $\theta$ , that define the chiral vector  $\mathbf{C}_h = n\mathbf{a}_1 + m\mathbf{a}_2$ . The tubes can then be identified using pairs of integers ( $n, m$ )<sup>19</sup> that define the chiral vector.

Carbon nanotubes have been found to assemble in bundles where the tubes are in a hexagonal array<sup>20,21,22</sup> with different lengths. Adsorption of simple gases on nanotubes bundles has been studied with different purposes. For example, Calbi et al.<sup>23,24</sup> studied the phases of neon, xenon, argon, hydrogen, and methane on the external surface of a nanotube bundle using numerical simulations. Zambano et al.<sup>25</sup> determined the experimental adsorption isotherms of xenon on bundles of closed SWNT and concluded that Xe adsorbs only on the outer surface of the bundles. Muris et al.<sup>26,27</sup> determined the adsorption isotherms of Xe, CF<sub>4</sub>, SF<sub>6</sub>, and Kr on single-walled nanotubes. They found stepwise isotherms and concluded that methane can

adsorb on the external grooves and in the widest interstitial channels between the tubes, whereas CF<sub>4</sub> and SF<sub>6</sub> can only adsorb on the outer surface of the bundles; they also suggested that there is a molecular sieve effect of the interstitial channels. Yin et al.<sup>28</sup> studied the adsorption of nitrogen on square arrays of open and closed single-walled nanotubes with different diameters. They concluded that the adsorption isotherms, in closed tubes with small tube separations, are of type I. In the case of open tubes, the extent of filling of the adsorption space is dominated by the tube diameter and the separation between tubes. Wang et al.<sup>29</sup> compared computer simulations of the adsorption of hydrogen on SWNT with the adsorption on model carbon slit pores. They found that carbon slit pores have a larger hydrogen adsorption capacity than the nanotubes. Mackie et al.<sup>30</sup> studied the adsorption of methane on carbon nanotubes and carbon filaments. They found that the untreated nanotubes give isotherms without hysteresis, whereas the treated samples give well-developed hysteresis loops. They concluded that the expected 1D behavior of the adsorbate in the nanotubes occurs for tube diameters smaller than 10 nm. In addition, they studied the wetting behavior of methane and concluded that this adsorbate completely wets the tubes in the liquid phase, whereas it incompletely wets the tubes in the solid phase.

Recently, Du et al.<sup>31</sup> studied the pore structure of single-walled carbon nanotubes using nitrogen and argon physisorption. They found that pristine samples contain variable amounts (15–38%) of open nanotubes. Their analysis of the pore size distribution is based on the Horvath–Kawazoe method that appears to be sensitive to species adsorbed in the outer grooves. Zhao et al.<sup>32</sup> calculated the binding energy of several gases adsorbed on SWNT using first principle methods. The values they have obtained for nitrogen are of the same order of magnitude as the ones reported in this work.

Computer simulations and experimental results have been compared in recently published papers. For example, Alain et al.<sup>33</sup> studied exohedral and endohedral nitrogen adsorption on model SWNT forming a square array. They compared the

\* To whom correspondence should be addressed. E-mail: ebottani@inifta.unlp.edu.ar. Phone: 54-221-425-7430. Fax: 54-221-425-4642.

simulations with the experimental isotherms achieving a good agreement between both results. In their opinion, interstitial adsorption seems to be very important. However, the adsorption capacity obtained experimentally does not reach the levels predicted by the simulations. This discrepancy could be due, in their opinion, to insufficient purification of the nanotubes samples and to a failure in the model, particularly in the assumption of a square array of the tubes. Fujiwara et al.<sup>34</sup> reported results of adsorption and X-ray diffraction studies of nitrogen and oxygen on SWNT bundles. They compared the adsorption on the as-produced tubes with the same sample heat-treated. In the first case, the tubes are closed while the heat treatment opens them. The original sample only adsorbs in the interstitial channels and the isotherms are Langmuir-type. The heat-treated sample adsorbs mostly in the inside of the tubes at low pressures while at higher pressures the interstitial channels are preferred. Murata et al.<sup>35</sup> compared simulations and experimental results for nitrogen adsorption on carbon nanohorn assemblies. They characterized the effect of thermal treatments, which through a partial oxidation create windows on the tube walls. The  $\alpha_s$  plot shows the presence of three kinds of sites: interstitial, intraparticle monolayer site, and an interparticle core site. The adsorption on intraparticle sites begins after the micropore filling of the stronger sites.

In this paper, we compare grand canonical ensemble Monte Carlo simulations of nitrogen adsorption at 77.5 K on single-walled carbon nanotubes bundles with experimental results both obtained in our laboratories and published in the literature. The sample employed to determine the adsorption isotherms has been characterized with several techniques (STM/AFM, TG, DTA, elemental analysis, X-ray diffraction, and SEM/EDX).

Several model solids have been studied all consisting of bundles of nanotubes in a hexagonal array. A detailed description of the structure of the solids is presented as well as the behavior of the interaction potential employed to calculate the gas–solid interaction energy. Additional simulations have been performed at 50, 63, and 120 K to characterize the adsorption process. The density profiles of the adsorbed phase are discussed and the average density of the adsorbed phase is calculated inside the tubes. The total isotherm is decomposed in local isotherms comprising in-tube, interstitial, and the bundles' external surface regions. The density profiles as a function of the distance to the reference plane are discussed to show how adsorption progresses. The distributions of molecules over the gas–solid energies are calculated and employed to identify the location of the adsorption sites within the simulation box. BET surface areas are also discussed and the effective radii of the tubes are calculated from the isotherms and compared to the values obtained from geometric arguments. The structure of the adsorbed phase within the tubes is also analyzed.

### Technical and Experimental Details

Single wall nanotubes produced by electric arcing of graphite in the presence of Ni–Y catalysts and manufactured by Nanolegde were used without further purification.

Atomic force and scanning tunneling microscopy (AFM/STM) investigations of the carbon nanotubes using highly oriented pyrolytic graphite (HOPG) as supporting substrate were accomplished.<sup>36,37</sup> A few mg of the SWNT material were dispersed in acetone using an ultrasonic bath. A drop of the suspension thus prepared was deposited onto a freshly cleaved HOPG surface and subsequently allowed to dry in air. The AFM/STM observations of the HOPG-supported nanotubes were carried out under ambient conditions in a Nanoscope Multimode

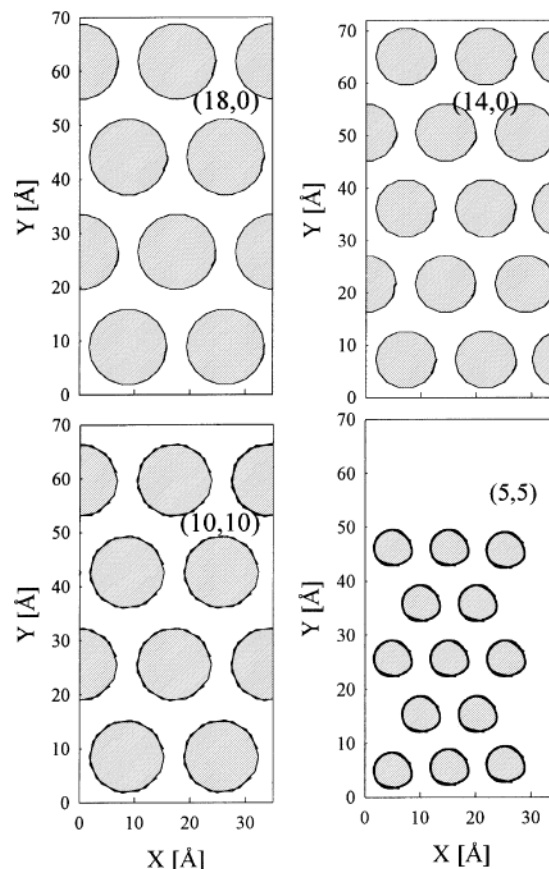


**Figure 1.** Schematic representation of the simulation cells.

IIIa apparatus, from Digital Instruments (Santa Barbara, CA). AFM imaging was performed in the tapping mode of operation, employing rectangular silicon cantilevers with resonance frequencies around 250 kHz and collecting images at constant amplitude of cantilever oscillation. Regarding STM, mechanically prepared Pt/Ir (80/20) tips were used. Typical tunneling parameters were 500 mV and 400 pA for the bias voltage and tunneling current, respectively. The STM images were acquired in the constant current mode (variable height).

Monte Carlo numerical simulations have been performed in the grand canonical ensemble and the algorithm has been described elsewhere.<sup>38</sup> To calculate the equilibrium properties, the necessary configurations of the system were generated. Each point is the result of  $9 \times 10^8$  creation/destruction and displacement attempts except for the first point of each simulation run where  $2.7 \times 10^9$  attempts were employed. The ratio of acceptance for creation/destruction was kept equal to ca. 1–2% and 45–50% for displacements. Each displacement includes a change in the orientation of the adsorbate. The simulation boxes employed to model the SWNT bundles are shown in Figure 1, and their dimensions are included in Table 1. Periodic boundary conditions were applied in  $x$  and  $y$  directions, and a reflection plane closed the box by the upper side. The bottom of the box was a uniform, nonadsorbing plane where the nanotubes were placed in a hexagonal array. The separation distance between nanotubes was 0.335 nm in all cases. The diameter of each nanotube has been determined using the well-known relation<sup>19</sup>

$$d_t = \frac{\sqrt{3}}{\pi} d_{C-C} (m^2 + mn + n^2)^{1/2} \quad (1)$$

where  $d_t$  is the geometric diameter of the tube measured from the center of a carbon atom,  $d_{C-C} = 0.144$  nm is the carbon–

**TABLE 1: Geometric Diameters,  $d_t$ , and Characteristics of the Nanotubes<sup>a</sup>**

$(n,m)$	nanotube type	$d_t$ [nm]	$L$ [nm]	$S_{\text{BET}}$ [nm <sup>2</sup> ]	$X$ [nm]	$Y$ [nm]
5,5	armchair—chiral	0.69	1.107	8.00	3.5	7.0
10,10	armchair—chiral	1.37	1.107	24.77	3.41	6.82
14,0	zigzag	1.11	0.923	17.82	3.61	7.22
18,0	zigzag	1.43	0.923	21.76	3.53	7.06

<sup>a</sup>  $(n,m)$  are the components of the chiral vector,  $L$  is the length of the tubes, and  $X$  and  $Y$  are the cell dimensions. The last column shows the BET areas obtained from the simulated isotherms.

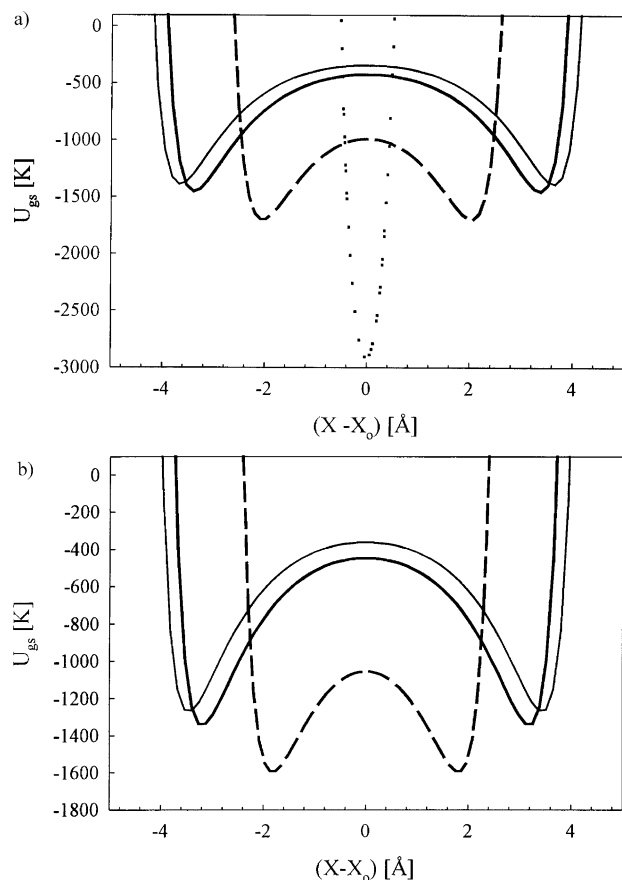


**Figure 2.** Gas—solid energy for a nitrogen molecule adsorbed in the tubes as it moves on the  $x$  direction keeping constant  $y$  and  $z$ . ( $5 \times 5$ ): dotted line; (10,10) thicker full line; (14,0) broken line; and (18,0) thinner full line. (a) Molecular axis parallel to the cylinder axis; (b) molecular axis perpendicular to the cylinder axis.  $X_0$  is the center of the tube coordinate.

carbon bond length, and  $n$  and  $m$  are the integers that define the chiral vector. Four nanotubes have been modeled, two armchair tubes and two zigzag tubes. The geometric diameters and the lengths of each tube are indicated in Table 1. In the case of nanotubes (5,5), some empty space was left in the simulation box to analyze the adsorption on the lateral surface of the bundle.

The interaction energy between the adsorbate and the solid was calculated using a Lennard-Jones (6,12) potential function, and the corresponding parameters were  $\epsilon_{\text{gs}} = 31.5$  K and  $\sigma_{\text{gs}} = 0.336$  nm that have been previously employed with the system nitrogen—graphite.<sup>39</sup> Figure 2 shows the gas—solid energy for a nitrogen molecule adsorbed into the tubes (Figure 2a corresponds to the adsorbate with its molecular axis parallel to the tube main axis, and Figure 2b was calculated for the molecule with its axis perpendicular). It can be noted that (5,5) nanotubes cannot hold a nitrogen molecule with its molecular axis

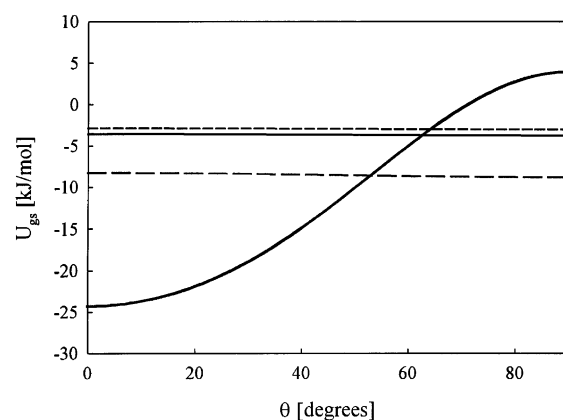


**Figure 3.** Gas—solid energy for an isolated molecule placed in the center of the tube as a function of the azimuthal angle. ( $5 \times 5$ ): thicker full line; (10,10) thinner full line; (14,0) dash-dotted line; and (18,0) broken line.

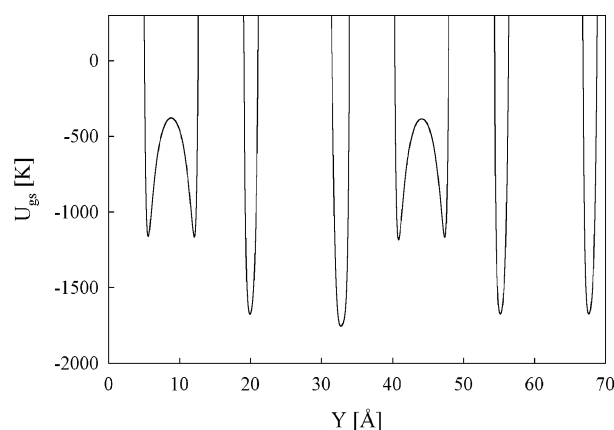


**Figure 4.** Gas—solid energy as a function of the  $y$  coordinate for an isolated molecule crossing through the simulation box corresponding to (18,0) tubes bundle. The molecule is with its molecular axis perpendicular to the tube axis and  $z = 0.5$  nm. The deepest and narrowest potential wells correspond to the interstitial regions between tubes.

**TABLE 2: Gas—Solid Energy Minima for an Isolated Molecule Adsorbed in the Nanotubes for Two Extreme Orientations, Molecular Axis Perpendicular to the Axis of the Tube and Parallel to This Axis ( $z = 0.5$  nm)**

tube	energy minima [kJ/mol]		average [kJ/mol]
	parallel	perpendicular	
(5,5)	−24.3		−24.3
(14,0)	−14.1	−13.2	−13.65
(10,10)	−12.1	−11.1	−11.6
(18,0)	−11.4	−10.5	−10.95

perpendicular to the cylinder axis. Table 2 summarizes the energy minima obtained for all of the solids studied that will be discussed later on. These results agree with the profiles shown in Figure 3 where the gas—solid energy of an isolated molecule, placed in the center of the tubes, is represented as a function of the azimuthal angle. The molecule can adopt any orientation in all tubes except in tube (5,5) where the energy becomes unfavorable as the azimuthal angle approaches  $70^\circ$ . Figure 4 shows the changes in gas—solid energy as a molecule, with the molecular axis parallel to the tube axis, is displaced through the simulation box at constant  $z$  and  $x$  for tube (18,0) as an example. In this figure, several minima in the gas—solid energy can be easily identified corresponding to the molecule within the tubes and in the interstitial regions between tubes. In all cases, the interstitial regions exhibit a deep and narrow well

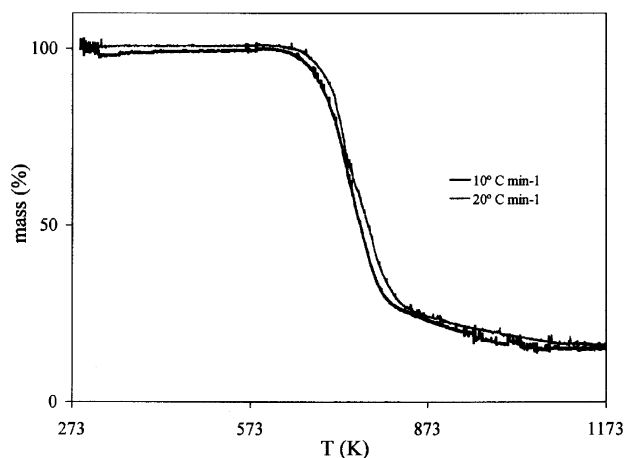


**Figure 5.** Thermogravimetry performed with synthetic air of the SWNT sample at two different heating rates.

depth suggesting that the adsorption on these regions will be restricted as in the interior of the tubes. These adsorption energy values will be very difficult to be observed in the simulations where, because of thermal energy, the molecular axis is randomly tilted with respect to the tube axis (this effect lowers the adsorption energy).

Nitrogen molecules have been modeled as a set of two Lennard-Jones interaction sites separated at 0.110 nm, and nitrogen–nitrogen interactions were calculated using  $\epsilon_{\text{gg}} = 36.4$  K and  $\sigma_{\text{gg}} = 0.332$  nm. The nitrogen quadrupole moment was taken into account and modeled by placing two charges on each nitrogen atom and one on the center of mass of the molecule. The magnitude of the charges was such that the quadrupole moment was equal to the experimental value.<sup>39</sup>

The adsorption isotherms determined in our laboratory were obtained using an ASAP 2010 automatic apparatus (Micromeritics). The sample of nanotubes was degassed at 523 K overnight prior to isotherm measurements and its BET surface area was  $329.4 \pm 0.8$  m<sup>2</sup> g<sup>-1</sup>.

Elemental analysis was performed in a LECO CHNS-932 microanalysis apparatus with a LECO VTF-900 accessory for oxygen. The elemental analysis of the employed sample (wt %, dry basis) gave 87.90% C, 0.43% H, 0.65% N, and 1.52% O, with ca. 12.50% ash content.

A Stanton-Redcroft STA-1500 thermobalance provided with a Plus-V software was used for simultaneous thermogravimetry (TG)/differential thermal analysis (DTA) measurements. A synthetic air constant flow of 50 cm<sup>3</sup> min<sup>-1</sup> was used. Temperatures were measured with Pt/Rh thermocouples placed at the bottom of the Pt crucibles, in contact with them.  $\alpha$ -Alumina was the reference material for DTA measurements. Figures 5 and 6 show the TG and DTA curves, respectively, obtained with linear heating rates of 10 and 20 K min<sup>-1</sup> over the temperature interval 298–1173 K. The residue at 1173 K of ~15wt % should be due to metal impurities in the sample. The highest heating rate allows distinguishing two exothermal processes (with maxima centered at 729 and 783 K) in the combustion of the sample. These two processes must be related to different types of carbonaceous fractions in the material: the more graphitic, the less reactive the carbonaceous material will be.

To complete the characterization of the sample employed in this work, X-ray diffractograms were measured on a Siemens D5000 instrument. Copper K $\alpha$  radiation ( $\lambda = 1.5406$  Å) at 40 kV and 30 mA was used as an X-ray source. Samples were scanned in the transmission mode in a set-scan mode (0.015°) and 3 s at each step. The dominant peak of SWNT, assigned to

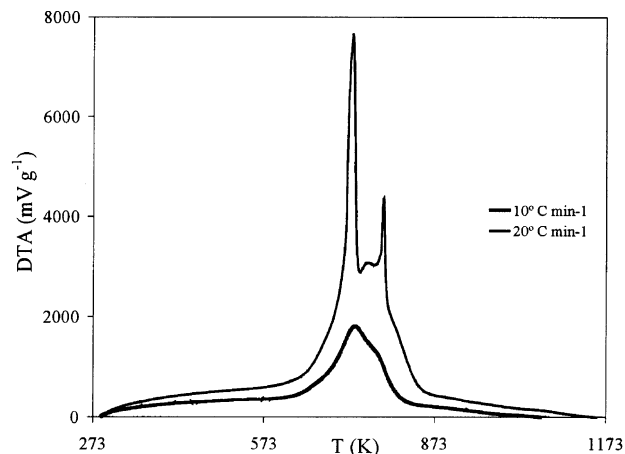


**Figure 6.** Differential thermal analysis curves simultaneously obtained with the TG ones.

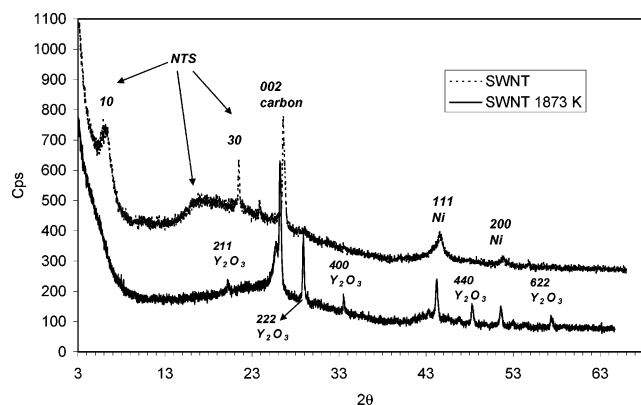


**Figure 7.** X-ray diffraction patterns of the pristine and heat-treated samples at 1873 K. Peak assignment is indicated in the figure.

the 10 reflection, occurs near  $s = 0.07$  Å<sup>-1</sup> which leads to a lattice parameter equal to 1.42 nm and an average tube diameter equal to 1.1 nm, assuming a van der Waals gap of 0.32 nm between tubes.<sup>40</sup> SWNT are assembled into bundles around 9–10 nm in diameter. A peak, very broad, is centered near  $s = 0.19$  Å<sup>-1</sup> ( $hkl = 21$ ). The dominant peak in the XRD,  $s = 0.3$  Å<sup>-1</sup> ( $hkl = 002$ ), is assigned to carbon (graphite) with a lattice parameter = 3.343 Å. Another peak centered near  $s = 0.24$  Å<sup>-1</sup>,  $hkl = 30$ , is also ascribable to carbon nanotubes.<sup>41</sup> The other dominant peaks in the XRD were assigned to the 111 and 200 reflections of Ni. After heat treatment at 1873 K, the sample is characterized by the disappearance of most of the  $hk0$  (10, 30) reflections in the XRD assigned to SWNT and increase of the lattice parameter  $s = 3.354$  Å<sup>-1</sup> ( $hkl = 002$ ) assigned to carbon, meaning a significant decrease of the crystalline order. Other peaks in the XRD were assigned to 211, 222, 440, and 622 reflections of Y<sub>2</sub>O<sub>3</sub>. Our results do not agree with what has been recently reported by Méténier et al.<sup>41</sup> In fact, they claimed that heating a nanotubes sample at 1873 K did not result in changes in the X-ray diffractogram, whereas heating at 2073 K produced the disappearance of the peaks assigned to the nanotubes in the diffractogram. On the other hand, our results (see Figure 7) show that heating the sample at 1873 K produced the disappearance of the nanotube peaks, the appearance of peaks corresponding to Y<sub>2</sub>O<sub>3</sub>, and the enhancement of the peaks assigned to Ni. This interpretation agrees with recently published data obtained by Chattopadhyay.<sup>42</sup> These authors showed that aggressive chemical and thermal treatments must be performed to completely remove the impurities.



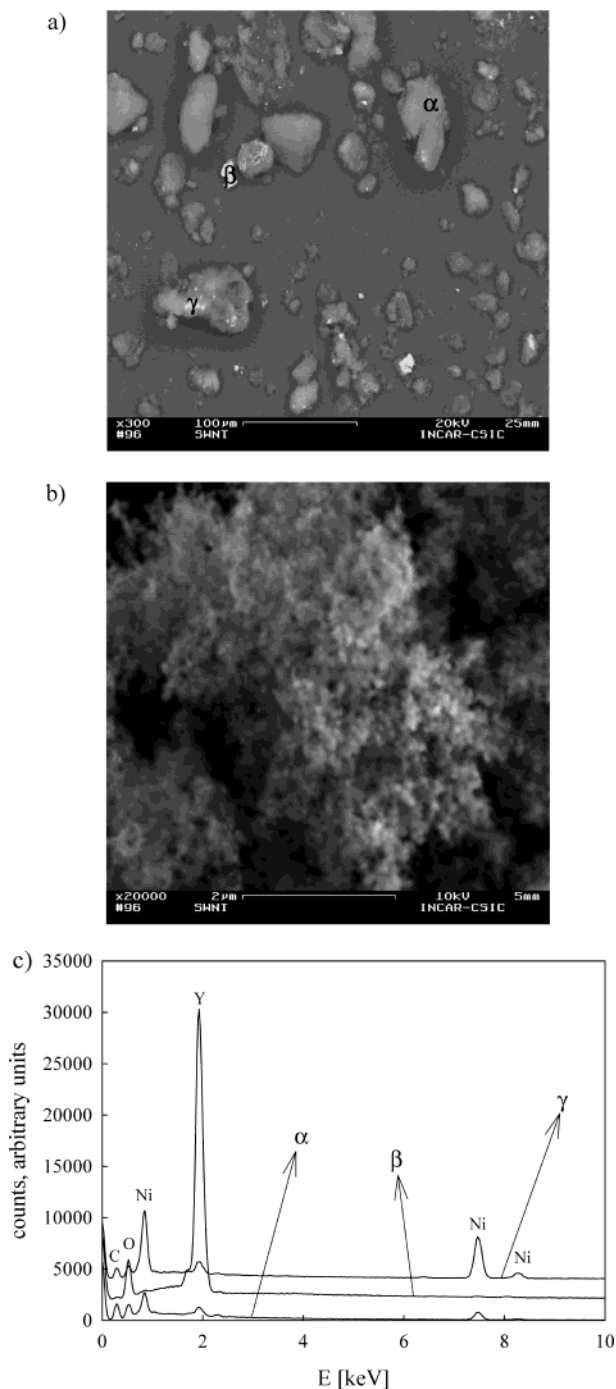


**Figure 8.** SEM micrographs of the SWNT sample at two different resolution levels (a,b) and EDX spectra (c) taken at different areas indicated in micrograph a.

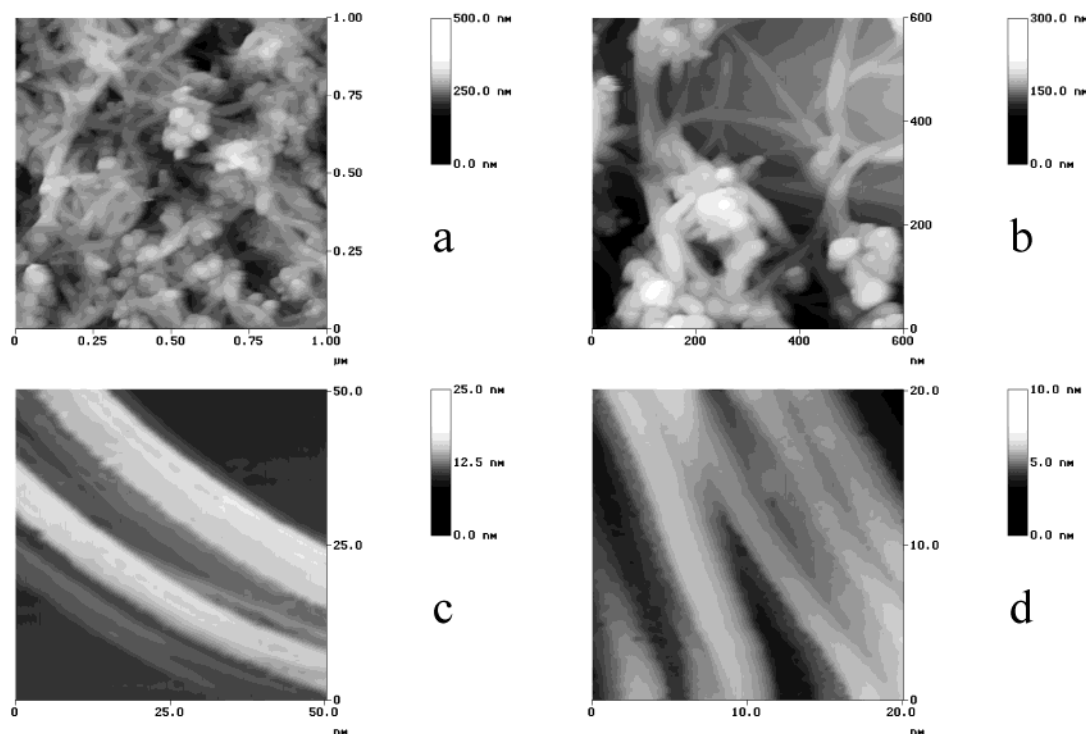
SEM-EDX studies were conducted using a scanning electron microscope Zeiss DSM-942, provided with an ultrathin Si/Li window detector for EDX microanalysis Link-ISIS. Samples were used in powder form and were not covered with any coating in order to avoid obtaining spurious signals in the microanalysis. Figure 8a shows a SEM micrograph of the studied carbon nanotube sample obtained at low resolution. The material consists of a mixture of phases of different brightness. The spectrum denoted as  $\alpha$  in Figure 8c was taken from the dark particle indicated as  $\alpha$  in Figure 8a and corresponds to the carbonaceous matter constituting the nanotubes. Figure 8b is a high-resolution SEM micrograph corresponding to one of the carbon-rich dark particles and shows that they consist of spongy masses.

Bright particles in the SEM micrographs consisted of catalysts remaining from the preparation procedure. Thus, spectrum  $\beta$  in Figure 8c, which only contains Y and O, was obtained from the bright particle indicated with the same symbol in Figure 8a; the bright particle near the lower right corner of the same figure yielded a similar spectrum. It was found that yttrium (likely in the form of an oxide) was not associated to other elements. However, Ni was generally associated with C or Fe. For instance, spectrum  $\gamma$  in Figure 8c, taken from the brightest zone of the particle indicated with the same symbol in Figure 8a, contained Ni together with C, O, and some Y. Similar results were obtained with a sample thermally treated at 1873 K, indicating that, contrary to results from Bourguine et al.,<sup>43</sup> the catalysts cannot be eliminated by mere thermal treatment at 1873 K. The only clear effect of this high-temperature treatment was sintering and phase segregation; in fact, carbonaceous and catalytic particles were more easy to discern than in the fresh material.

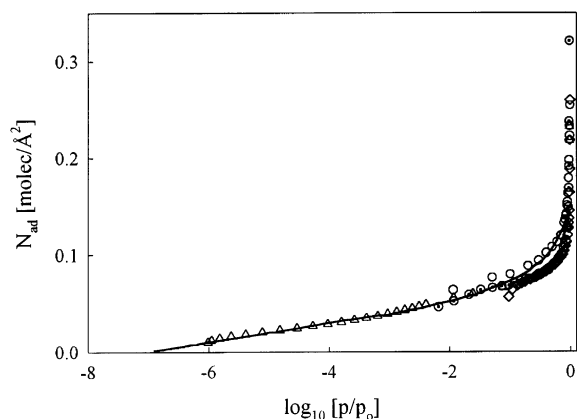
## Results and Discussion

Figure 9, parts a and b, shows two typical tapping mode AFM images of the SWNT sample. It can be noticed that nanotube bundles are intermingled with approximately spherical particles. These particles display diameters typically between 30 and 70 nm and are attributed to the amorphous carbon that forms during the production process of the nanotubes. In addition, some of them may be encapsulating the metal nanoparticles employed to catalyze the nanotube growth.<sup>5</sup> The nanotube bundles present diameters usually between 4 and 15 nm (measured as the height of isolated bundles on the HOPG substrate), which correspond to aggregates of several to a few tens of SWNTs. Occasionally, individual nanotubes were observed as well. Likewise, the nanotube bundles appeared in general essentially pristine (i.e., free of any traces of impurities), although in a few cases the presence of small bumps (about 1–2 nm high and several nm long) was noted on the surface of some bundles (images not shown). Phase contrast images revealed the bumps as regions where AFM tip-sample energy dissipation was enhanced compared to both the pristine areas of SWNT bundles and the HOPG substrate, which, in turn, would be consistent with the bumps being patches of disordered (amorphous) carbon.<sup>44</sup> Spots of amorphous carbon are also found sometimes by transmission electron microscopy (TEM) on the walls of SWNTs samples.<sup>45,46</sup>

Concerning the STM observations, Figure 9, parts c and d, shows two images of single bundles where individual SWNTs are resolved, as well as the narrow depressions (grooves) separating them. In Figure 9c, it can be seen that the nanotubes run parallel to each other, therefore comprising a well-arranged bundle, this being the type of structure where physisorption of nitrogen was simulated. It should be noted here that the STM images directly disclose one of the nitrogen adsorption sites considered in the simulations, i.e., the external grooves that lie between two adjacent, outer nanotubes. Furthermore, although they cannot be directly visualized, the presence of interstitial channels in the inner parts of the bundle (another type of the adsorption sites considered) is inferred from the STM images, because such inner channels can be thought of as formed when an outer groove between two nanotubes is closed by a third one. Although in general terms the SWNT bundles appeared tidily arranged, some packing imperfections were also detected. One example is shown in Figure 9d, where a wedge-shaped opening in the bundle is clearly noticed in the bottom half of the image. These defects were relatively abundant in the STM images and represented voids of several nm in the SWNT bundle



**Figure 9.** (a and b) AFM (tapping mode); (c and d) STM images of SWNT sample supported on HOPG employed to obtain the adsorption isotherms.



**Figure 10.** Nitrogen adsorption isotherms at 77.5 K. (○) from Murata et al.;<sup>35</sup> (◇) from Alain et al.;<sup>33</sup> (⊙) from Fujiwara et al.;<sup>34</sup> (—) simulations; (Δ) this work experiments.

structure, where, in consequence, capillary condensation is expected to occur. Therefore, the small hysteresis loop observed in the nitrogen adsorption isotherms (hardly visible in Figure 10 because of the employed scale) can be attributed at least in part to such imperfections. On the other hand, as visualized by STM, the rounded particles coexisting with the nanotubes were very similar in appearance to carbon black,<sup>47</sup> i.e., they exhibited an extremely smooth surface with no sign of micropores or mesopores, which suggests that they are nonporous carbon displaying only external surface.

The simulated isotherms are compared with the experimental ones in Figure 10. The data from Murata et al.<sup>35</sup> correspond to a sample of single-walled nanohorns heated at 573 K. This thermal treatment opens the tubes by creating windows on the walls and also opens the interparticle space through a partial oxidation of the material. The data from Alain et al.<sup>33</sup> correspond to a sample of nanotubes similar to our sample. Their nanotubes are closed because no thermal or oxidation treatments have been performed. The data taken from Fujiwara et al.<sup>34</sup> correspond to

a sample of SWNT heated in air at 623 K to open the tubes. It must be pointed out that the samples employed by Alain et al. and Fujiwara et al. have been obtained by the same method (evaporation of graphite rods containing Ni and Y in He atmosphere). The diameters of the tubes reported by those authors are close to the simulated tubes (5,5), (10,10), and (18,0). The line representing the simulated isotherms in Figure 10 is the result of a least-squares fitting of all of the simulations results. The areas employed to reduce the isotherms are the BET ones quoted in Table 1. The agreement between the simulations and the samples with open tubes is quite good particularly at low pressures where gas–solid interactions are dominant. As could be expected the isotherm corresponding to the closed tubes agrees with the others as saturation pressure is approached. The agreement between the simulations and the experimental data obtained in our laboratory is excellent up to relative pressures close to 0.2. Even though our simulations are performed considering open tubes and the experiments likely correspond to closed tubes, the agreement is not quite unexpected. The real sample was employed as-received and could contain a certain fraction of open tubes.<sup>31</sup> In the real system, adsorption should take place mostly in the interstitial spaces while in the simulations endohedral spaces compete with interstitial cavities. Nevertheless, both regions constitute restricted spaces of the same chemical nature; thus, the adsorption isotherms could be expected to coincide. At moderate relative pressures, the slight discrepancy between the simulations and our experimental data is mainly due to the endohedral adsorption in the simulated isotherms. This explanation is consistent with the fact that the simulation agrees with the experimental data obtained with the open tubes. Finally, the discrepancy between the simulations and experiments at relative pressures close to unity can be attributed to several reasons. In first place, our simulations are unable to reproduce the experimental data when the density of the system is close to the saturation.<sup>39</sup> The second reason is that the model bundles employed in the simulations are perfect

and have no impurities. From the side of the experimental data, besides the obvious possibility of experimental error, all samples contain impurities introduced during the preparation procedure. These impurities are mainly amorphous carbon particles containing the metal used as catalyst that can alter the isotherms. Finally, structural imperfections such as those shown in Figure 9 can also alter the isotherms. Our simulations do not show hysteresis, and the experimental isotherm obtained with our sample exhibits a rather small hysteresis loop. Both results are in agreement with results reported by other authors working with pristine samples.<sup>5</sup>

From the simulations, it is possible to calculate the adsorption isotherms over the entire surface excluding the interior of the tubes and to compare these results with the experimental data obtained for closed tubes. In this case, the simulated isotherms agree with the experimental ones up to relative pressures ca. 0.4. Three local adsorption isotherms have been calculated that we called in-tube corresponding to the interior of the tubes, inter-tube corresponding to the interstitial space between tubes, and out-tube corresponding to the external surface of the bundle. The obtained isotherms are displayed in Figure 11a–c. As could be expected the isotherms on the restricted spaces reach saturation and the isotherms belong to type I in IUPAC classification. The in-tube isotherms reach saturation in the sequence determined by the diameter of the tubes as could be anticipated. The sequence for the interstitial adsorption also agrees with the different sizes of these spaces. The saturation limits also indicate that the adsorption capacity of the tubes is almost the same as the interstices one. The isotherms on the external surface are s-shaped and they exhibit the usual features.

From gas adsorption experiments, it is possible to determine the effective pore width,  $w$ , given by<sup>48</sup>

$$w = H - (2z_0 - \sigma_{\text{gg}}), \quad z_0 = 0.856\sigma_{\text{gs}} \quad (2)$$

where  $z_0$  is related to the gas–solid potential size parameter,  $\sigma_{\text{gs}}$ ,  $H$  is the diameter of the tube measured between the center of carbon atoms, and  $\sigma_{\text{gg}}$  is the gas–gas potential size parameter. From the local isotherms corresponding to the in-tube adsorption, and assuming that the adsorbed phase within the tubes at saturation is liquidlike, it is possible to calculate the effective diameter of the tubes. The results obtained with eq 2 and the local isotherms are summarized in Table 3. The effective diameters calculated with eq 2 are always larger than the estimates obtained from the isotherms. This difference, which amounts in average to 15%, can be attributed to several reasons starting with the interaction parameters, eq 2 itself, and the fact that the state of the adsorbed phase could be other than liquidlike. This last reason is probably the right one given the diameters of the nanotubes. Bojan et al.<sup>49</sup> estimated the diameter of rough-walled cylindrical pores using as criterion the fact that there could not be adsorbed molecules closer to the pore wall than  $\sigma_{\text{gs}}/2$ . We have applied this definition by means of a rough estimation from the curves shown in Figure 2. The results are very similar to those obtained with eq 2. It is possible to calculate the density of the adsorbed phase if we accept as correct the number of molecules adsorbed at saturation in the tubes, obtained from the local isotherms, and using the effective volume of the tubes. The average value obtained is  $0.0122 \pm 0.0003$  molecules/ $\text{\AA}^3$  which is lower than the experimental value for liquid nitrogen ( $0.0173$  molecules/ $\text{\AA}^3$ ). As could be expected, nitrogen molecules adsorbed in the confined space do not pack as in the liquid. Another interesting result concerns the monolayer capacity determined with the BET method applied to the local isotherms and its comparison with values from other

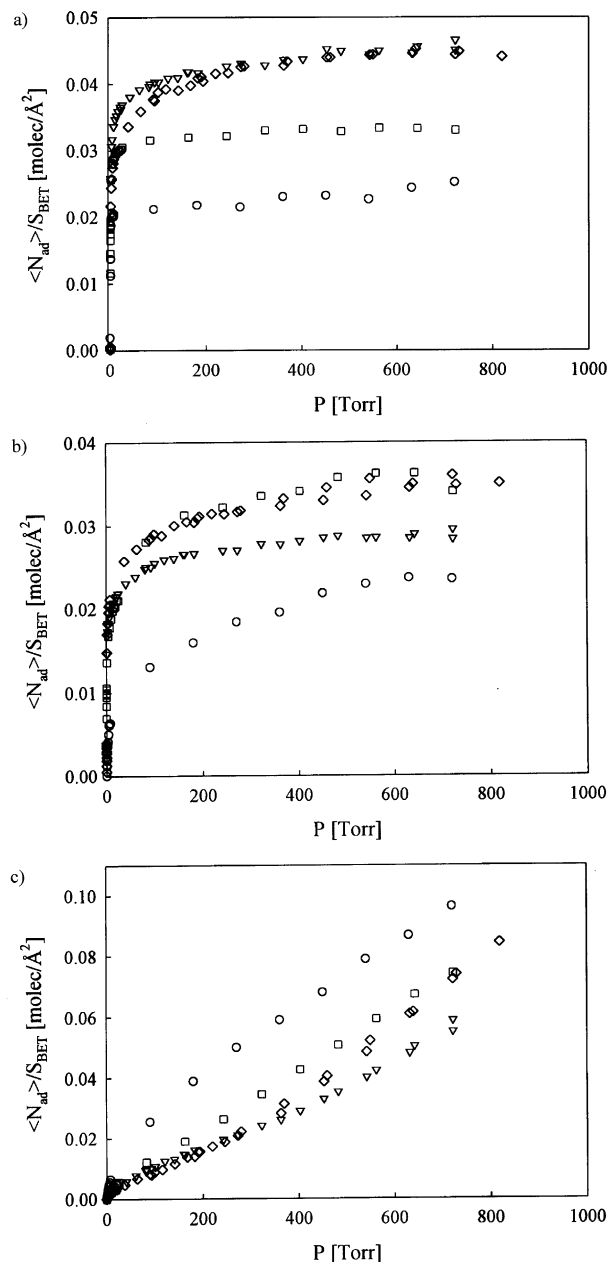


**Figure 11.** Nitrogen local adsorption isotherms at 77.5 K. (a) in-tube adsorption; (b) adsorption on the interstitial space; and (c) out-tube adsorption. (○) (5,5); (◇) (18,0); (▽) (10,10); and (□) (14,0).

**TABLE 3: Comparison of Effective Tube Diameters Calculated with Equation 2 ( $w$ ) and the Values Obtained from the Adsorption Capacity at Saturation ( $w_{\text{calc}}$ ) [ $\sigma_{\text{gs}} = 0.336$  nm and  $\sigma_{\text{gg}} = 0.332$  nm]**

tube	$H$ [nm]	$w$ [nm]	$w_{\text{calc}}$ [nm]
(5,5)	0.69	0.45	0.39
(10,10)	1.37	1.13	0.97
(14,0)	1.11	0.87	0.74
(18,0)	1.43	1.19	0.97

sources, i.e., estimates obtained with geometric arguments, and from the saturation limit reached by the isotherms. The obtained values are summarized in Table 4. The average discrepancy found, approximately 28%, could be expected because the BET method applicability is doubtful in the case of microporous solids.<sup>50</sup>

The total potential energy of the adsorbed molecules behaves as could be expected for heterogeneous solids as can be seen in Figure 12. A rough extrapolation at zero coverage produces

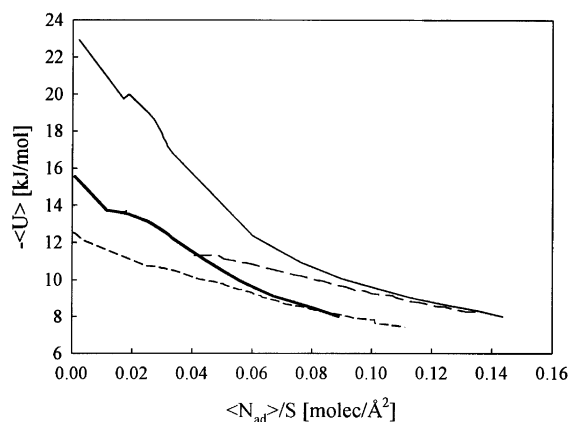


**Figure 12.** Total potential energy for nitrogen adsorption at 77.5 K on nanotubes bundles. (5,5) Full thinner line; (14,0) full thicker line; (10,10) long-dashed line; (18,0) short-dashed line.  $S$  is the BET surface area obtained from the adsorption isotherms.

**TABLE 4: Comparison of the Monolayer Capacity Obtained with the BET Method ( $N_{\text{BET}}$ ) with the Value Deduced from the Geometry of the Tubes ( $N_{\text{geo}}$ ) and the Value Obtained from the Local Isotherms ( $N_{\text{iso}}$ )**

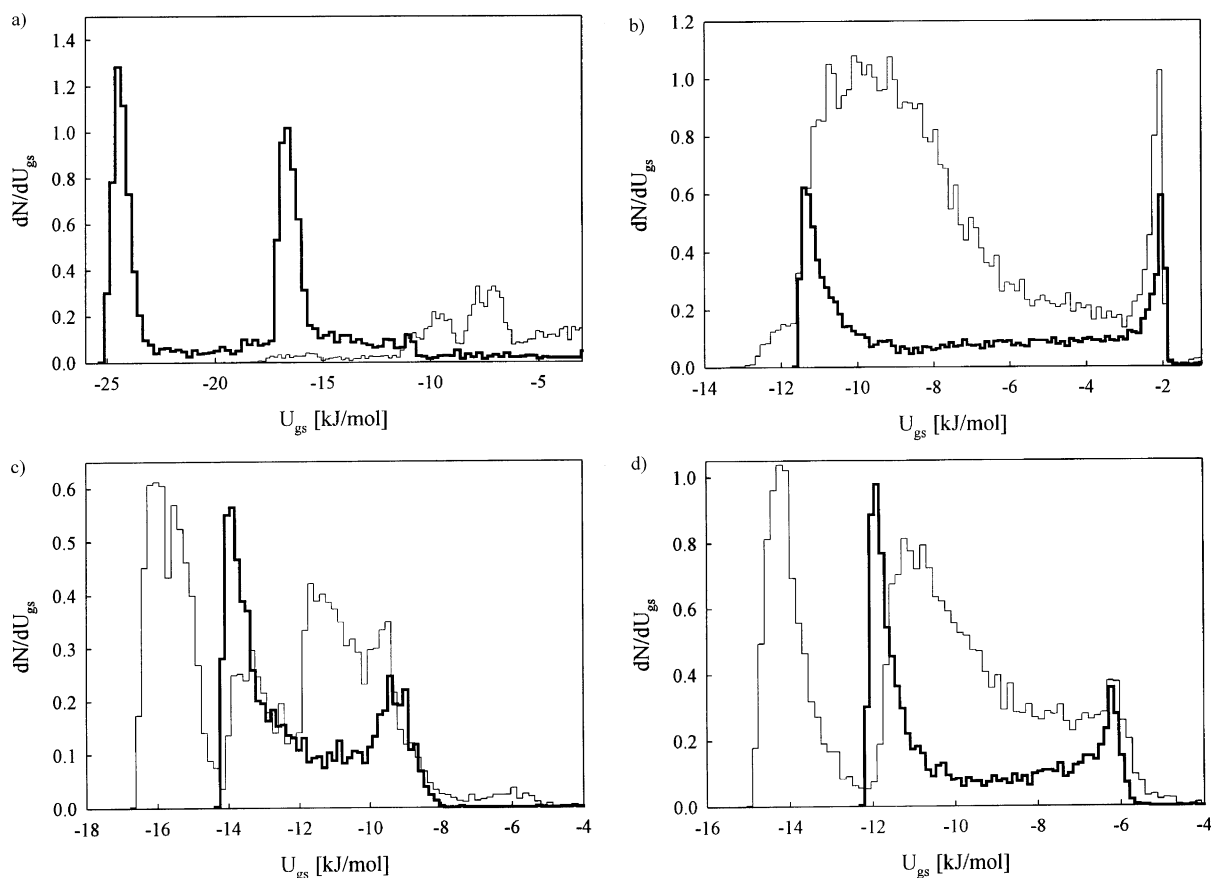
tube	$N_{\text{BET}}$ [molec.]	$N_{\text{geo}}$ [molec.]	$N_{\text{iso}}$ [molec.]
(5,5)	49.7	56.9	20
(10,10)	153.2	152.9	113
(14,0)	109.7	83.9	60
(18,0)	138.4	138.6	97

energy values that are consistent with the values quoted in Table 2. The limiting value of the energy at high surface coverage is larger than the usual values obtained for other heterogeneous

carbonaceous materials (liquid nitrogen vaporization enthalpy) suggesting that the adsorbed phase is not liquidlike or it is a consequence of the porous nature of the nanotubes bundles.

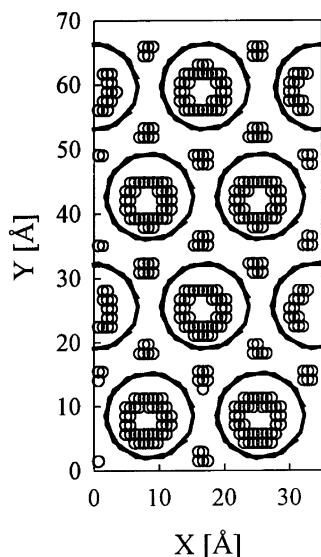
From the simulations, it is possible to calculate the distributions of adsorbed molecules according to the gas–solid energy. Figure 13a–d shows the obtained distributions for molecules adsorbed inside the tubes and out of them. These distributions have been obtained averaging over all of the equilibrium configurations generated during the simulations. For each configuration, molecules inside and outside the tubes were identified and their gas–solid energy was calculated. The distributions can be interpreted with the aid of the results shown in Figures 2a–b and 3. These distributions present common features as could be expected. In fact, molecules in the tubes exhibit two peaks in the distribution, one corresponding to the molecules near the wall and a second one corresponding to additional molecules in the center of the tube (when the tube diameter is large enough to allow this situation, which is not the case for (5,5) tubes). The distributions corresponding to molecules adsorbed outside the tubes resemble the ones obtained for the adsorption on irregular surfaces. In some cases, it is possible to speculate about the existence of unresolved peaks. Those peaks should correspond to the adsorption on the interstitial spaces and on the external walls of the bundle, more precisely on the grooves formed by three nanotubes.<sup>34,48</sup>

Figure 13a shows the distributions obtained for (5,5) tubes bundle. The distribution of molecules inside the tubes shows two well-resolved peaks, one located at ca.  $-24$  kJ/mol that corresponds to a molecule in the center of the tube (see Figure 2a) with the molecular axis parallel to the axis of the tube. The second peak is approximately at  $-16$  kJ/mol and can be assigned



**Figure 13.** Distributions of molecules according to the gas–solid energy at 77.5 K. Adsorbed molecules are classified as being adsorbed in the tubes and out of them. In all cases, the thicker line corresponds to the endohedral adsorption and the thinner one to exohedral molecules. (a) (5,5); (b) (18,0); (c) (14,0); and (d) (10,10).





**Figure 14.** Average coordinates of adsorbed molecules at 77.5 K with gas–solid energy between  $-12.3$  and  $-9.4$  kJ/mol. The lines correspond to the projection of the coordinates of the nanotubes (10,10). The small circles denote the coordinates of the mass center of the adsorbate.

to molecules in the center of the tube but with their molecular axes tilted with respect to the cylinder axis. From Figure 3, the tilt angle can be estimated to be ca.  $40\text{--}45^\circ$ . These results could be indicating that molecules inside the (5,5) nanotubes are arranged in alternate orientations in such a way that gas–solid and gas–gas interactions are optimized. In the case of the other tubes (Figure 13b–d), two peaks are also observed, one corresponds to nitrogen molecules adsorbed on the walls of the tubes and the second one corresponds to the molecules in the center of the tube. In both cases, nitrogen molecules are with the molecular axis parallel to the axis of the tube. This conclusion is derived from the energy profiles depicted in Figure 3. Because these tubes are wider than the (5,5) nanotube, the

energy does not depend on the orientation when the molecule is close to the axis of the nanotube (see Figure 3), and it is the gas–gas interaction that controls the relative orientation of the molecules. This is the reason the distributions show both peaks separated by nonnegligible densities in between. Moreover, it could be taken as an indication of the disorder degree of the adsorbed phase.

The distributions obtained for exohedral molecules are characteristic of heterogeneous surfaces; only in two cases (tubes (14,0) and (10,10)) a well-resolved peak is found that corresponds to the adsorption in the interstitial space, whereas the unresolved ones correspond to adsorption on the external surface of the bundle. A final remark concerning these distributions is that they depend on the adsorbed amount. The ones shown as examples have been calculated at surface coverages as close as possible. To verify the identification of the peaks, a simple analysis has been performed on the equilibrated configurations generated during the simulations. The gas–solid energy for each molecule of a given configuration has been calculated, and then if the energy was comprised in a given interval, the  $x,y$  coordinates of the molecules were stored. The process is repeated with all of the configurations and then averaged. Finally, with those average coordinates, a projection on the  $xy$  plane has been drawn where the nanotubes projections have also been included. The results obtained confirm the assignment of the peaks. Figure 14 shows as an example the case of nanotubes (10,10) for energies between  $-12.3$  and  $-9.4$  kJ/mol that correspond to the most energetic peak for endohedral adsorption and the intermediate one for exohedral adsorption. As can be seen in the figure, the corresponding sites are located inside the tubes on the walls and outside the tubes in the interstitial positions.

Figure 15a–c shows the average densities of the adsorbed phase as 2D contour maps. To construct these maps, the simulation box is divided in a mesh of arbitrary size, and the positions of the center of mass of the adsorbed molecules are analyzed during the simulation disregarding the  $z$  coordinate.

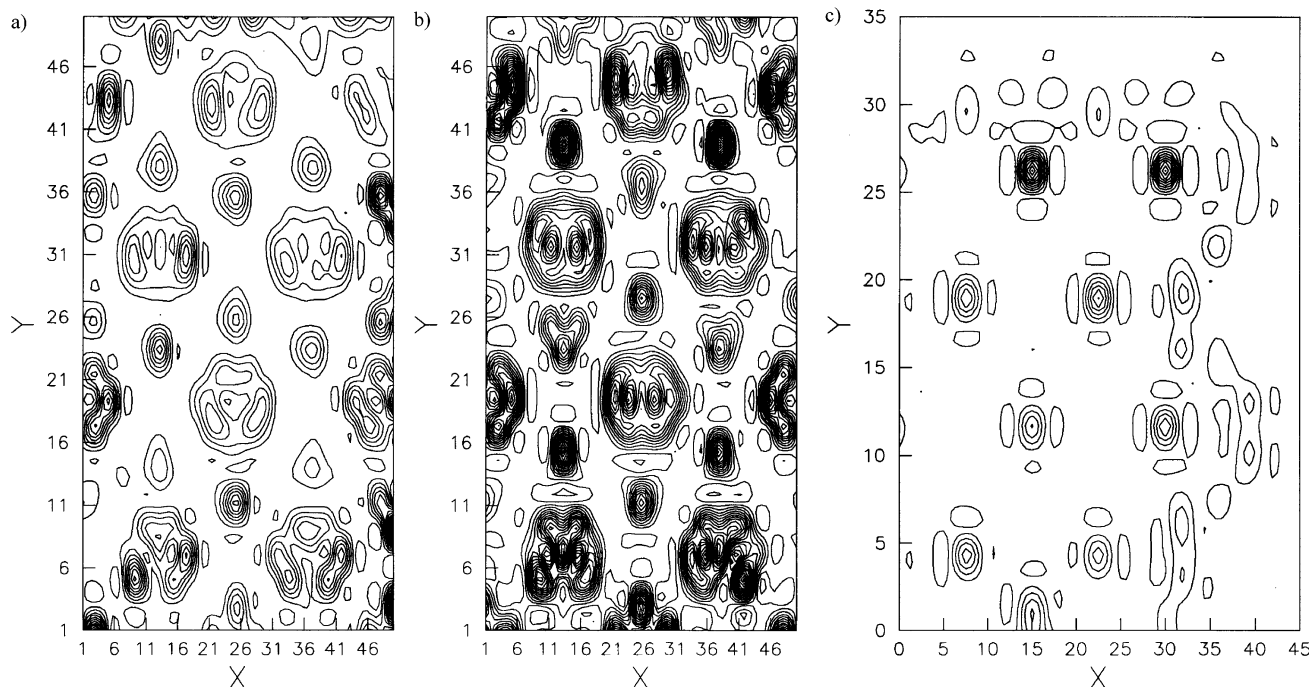


**Figure 15.** 2D maps of the average density of the adsorbed phase on three nanotube bundles taken as examples. (a) nanotube (10,10)  $\langle N_{\text{ad}} \rangle = 333.9$ ; (b) nanotube (18,0)  $\langle N_{\text{ad}} \rangle = 199.3$ ; and (c) nanotube (5,5)  $\langle N_{\text{ad}} \rangle = 115.1$ .  $x$  and  $y$  coordinates are in arbitrary units (1  $x$  unit =  $0.07$  nm; 1  $y$  unit =  $0.14$  nm).

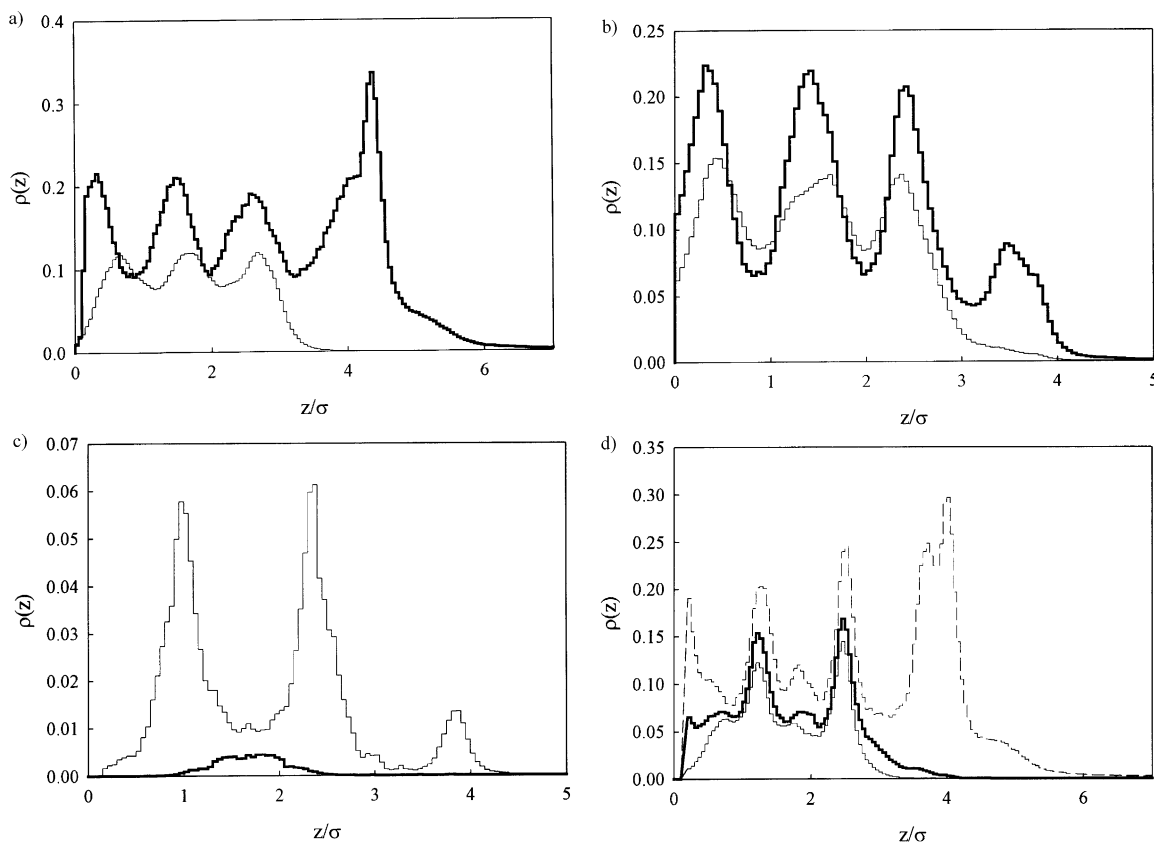


**Figure 16.** Density profiles as a function of the distance to the bottom of the simulation box obtained at 77.5 K for different adsorbed amounts. (a) (10,10) thick line  $\langle N_{\text{ad}} \rangle = 333.9$ , thin line  $\langle N_{\text{ad}} \rangle = 120.2$ ; (b) (18,0) thick line  $\langle N_{\text{ad}} \rangle = 199.3$ , thin line  $\langle N_{\text{ad}} \rangle = 139.5$ ; (c) (5,5) thick line  $\langle N_{\text{ad}} \rangle = 13.5$ , thin line  $\langle N_{\text{ad}} \rangle = 115.1$ ; (d) (14,0) thin line  $\langle N_{\text{ad}} \rangle = 73.6$ , thick line  $\langle N_{\text{ad}} \rangle = 101.5$ , and broken line  $\langle N_{\text{ad}} \rangle = 257.5$ . In all cases,  $\sigma = \sigma_{\text{gg}} = 0.332$  nm.

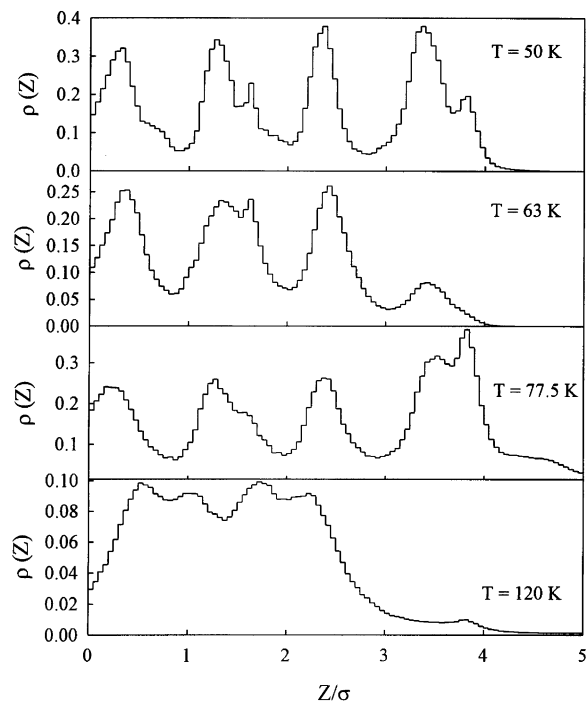


**Figure 17.** Density profiles for (18,0) nanotubes bundle calculated at different temperatures and approximately the same number of adsorbed molecules. In all cases,  $\sigma = \sigma_{\text{gg}} = 0.332$  nm.

The maps shown as examples have been obtained at different numbers of adsorbed molecules. In all cases, it is quite clear that the most preferred adsorption site is the interior of the nanotubes, followed by the interstitial sites, and finally the

external surface of the bundle. Moreover, on the exterior surface the sites are almost exclusively represented by the grooves formed by the nanotubes (Figure 9c), in agreement with what has been previously reported by other authors.<sup>23,24</sup> At low coverage (see Figure 15c), nonnegligible adsorption is observed in the interstitial regions and the external surface even when some nanotubes are not completely filled.

It is also interesting to analyze how the density of the adsorbed phase changes with the distance to the bottom of the simulation box for different adsorbed amounts. These profiles are obtained averaging over all of the configurations generated after equilibrium is reached for each point of the calculated isotherm. Figure 16a–d shows as examples several profiles obtained for all the nanotube bundles simulated. In all cases, the top of the nanotubes is at  $z/\sigma \approx 3.3$ . It must be pointed out that these profiles do not discriminate the molecules according to where they are adsorbed; thus, the observed peaks are due to both endohedral and exohedral adsorption. It is interesting to note that the separation between peaks is in average equal to  $1.1 \sigma_{\text{gg}}$ . This resembles the behavior found for nitrogen adsorption on a flat surface,<sup>51</sup> but the interpretation is different because in this case the adsorbate is mostly adsorbed in confined spaces (interior of the nanotubes and interstitial spaces). As a general rule, it can be said that the positions of the peaks are independent of the number of adsorbed molecules except for nanotubes (5,5) and (10,10) where a displacement is observed as the number of adsorbed molecules increases. This displacement is always toward the bottom of the tube. In all cases where a peak is found at  $z/\sigma < 1$ , it is due to the fact that the bottom of the simulation box is a nonadsorbing plane thus allowing the molecules to approach it without being repelled. The closest

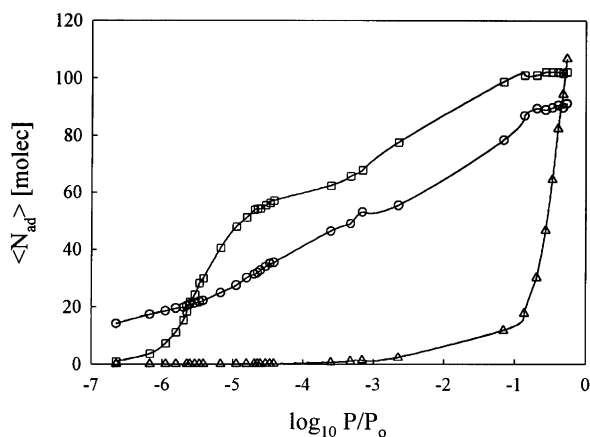


**Figure 18.** Nitrogen local adsorption isotherms on (18,0) nanotubes bundle at 50 K. (□) in-tube; (○) interstitial space; (△) out-tube adsorption.

approach distance is for the molecular center of mass being on this plane. The peak located at  $z/\sigma > 3.3$  corresponds to the adsorption on top of the nanotubes. Another characteristic of the profiles is that the peaks are not as sharp as in the case of a flat surface but are sharper than in the case of an amorphous surface. This general behavior is independent of the temperature as can be observed in Figure 17 where the density profiles calculated in a wide temperature range (50–120 K) are shown. The profile obtained at 120 K indicates a lack of order in the adsorbed phase. This is due to the larger kinetic energy of the adsorbed molecules.

Another interesting result arises from the analysis of the local isotherms obtained at different temperatures. Figure 18 depicts the obtained nitrogen isotherms for (18,0) nanotubes at 50 K where it can be seen that adsorption in the interstitial spaces is larger than in the tubes at the very low-pressure end of the isotherm. At higher pressures, depending on the temperature, in-tube adsorption becomes larger. The same behavior is observed at all temperatures studied. For the other tubes simulated, the endohedral adsorption is always larger until saturation is reached. It must be reminded that (18,0) nanotubes have the largest diameter among the series studied.

## Conclusions

The simulations reported here reproduce the experimental adsorption isotherms on SWNT of different diameters. The coincidence between experiments and simulations at low pressures is remarkably good. This situation persists until pore effects become more important. The disagreement between simulated and experimental isotherms at relative pressures close to saturation are due to inaccuracies in the calculation of the interactions between adsorbed molecules as well as experimental errors and problems associated with the degree of purity and perfection of the samples.

The effective diameters of the nanotubes obtained from the simulated isotherms are systematically smaller than the values deduced from eq 2. The adsorbed phase within the tubes exhibits a lower density than the bulk liquid even at saturation. This is a direct consequence of the diameter of the nanotubes. The distributions of molecules over the gas–solid energy show two peaks for endohedral adsorption. One of them is associated with molecules near the wall and the second one is due to molecules located close to the tube axis. In the case of (5,5) nanotubes, the observed peaks are due to molecules located along the tube axis with different tilt angles. The density profiles have several peaks that are consistent with the possible stacking of molecules

within the confined spaces (endohedral and interstitial). The positions of the peaks are independent of the number of adsorbed molecules except for nanotubes (5,5) and (10,10) where a displacement is observed. The total adsorption capacity of the interstitial channels is almost equivalent to that of the tubes at least for the solid simulated here.

The excellent agreement between the simulations and experiments suggests that the impurities present in real samples do not greatly affect the isotherms in the low-pressure limit. Nevertheless, they could be altering the experimental isotherms at moderate and high pressures. In favor of this argument is the fact that there is a large dispersion in the experimental data obtained on different samples, which is not found for other systems, and the evidences offered by the STM/AFM images presented in this work. Another problem concerning the experimental data is related to the purification method and the effect caused by thermal treatments in inert atmosphere, as has been shown by X-ray diffraction data. It has also been shown that simple thermal treatments do not remove metallic impurities as had been previously claimed. A systematic study is needed in this subject to characterize the samples employed and to ensure their quality.

**Acknowledgment.** E.J.B. is Associate Professor of the National University of “El Litoral” and researcher of the Comisión de Investigaciones Científicas de la Provincia de Buenos Aires. The research project is financed by Consejo Nacional de Investigaciones Científicas y Técnicas (CONICET), Comisión de Investigaciones Científicas de la Pcia de Buenos Aires (CIC) and Universidad Nacional de La Plata (UNLP). The Spanish team acknowledges financial support from DGI-CYT (Project PB98-0492).

## References and Notes

- (1) Iijima, S. *Nature* **1991**, 354, 56.
- (2) Colbert, D. T.; Zhang, J.; McClure, S. M.; Nikolaev, P.; Chen, Z.; Hafner, J. H.; Owens, D. W.; Kotula, P. G.; Carter, C. B.; Weaver, J. H.; Rinzler, A. G.; Smalley, R. E. *Science* **1994**, 266, 1218.
- (3) Ando, Y.; Zhao, X.; Hirahara, K.; Suenaga, K.; Bandow, S.; Iijima, S. *Chem. Phys. Lett.* **2000**, 323, 580.
- (4) Wang, X.; Lu, J.; Xie, Y.; Du, G.; Guo, Q.; Zhang, S. *J. Phys. Chem. B* **2002**, 106, 933.
- (5) Yang, C. M.; Kaneko, K.; Yudasaka, M.; Iijima, S. *Nano Lett.* **2002**, 2, 385.
- (6) Andrews, R.; Jacques, D.; Qian, D.; Dickey, E. C. *Carbon* **2001**, 39, 1681.
- (7) Chiang, I. W.; Brinson, B. E.; Smalley, R. E.; Margrave, J. L.; Hauge, R. H. *J. Phys. Chem. B* **2001**, 105, 1157.
- (8) Moon, J. M.; An, K. H.; Lee, Y. H.; Park, Y. S.; Bae, D. J.; Park, G. S. *J. Phys. Chem. B* **2001**, 105, 5677.
- (9) Ebbesen, T. W.; Ajayan, P. M. *Nature* **1992**, 358, 220.
- (10) Ebbesen, T. W.; Hiura, H.; Fujita, J.; Ochiai, Y.; Matsui, S.; Tanigaki, K. *Chem. Phys. Lett.* **1993**, 209, 83.
- (11) Ajayan, P. M. *Chem. Rev.* **1999**, 99, 1787.
- (12) Fischer, J. E. *Chem. Innov.* **2000**, October, 21.
- (13) Challa, S. R.; Sholl, D. S.; Jonson, J. K. *J. Chem. Phys.* **2002**, 116, 814.
- (14) Cheng, H.-M.; Yang, Q.-H.; Liu, C. *Carbon* **2001**, 39, 1447.
- (15) Adu, C. W. K.; Sumanasekera, G. U.; Pradhan, B. K.; Romero, H. E.; Eklund, P. C. *Chem. Phys. Lett.* **2001**, 337, 31.
- (16) Tibbetts, G. G.; Meisner, G. P.; Olk, C. H. *Carbon* **2001**, 39, 2291.
- (17) Talapatra, S.; Migone, A. D. *Phys. Rev. Lett.* **2001**, 87, 206106–1.
- (18) Maddox, M. W.; Gubbins, K. E. *Langmuir* **1995**, 11, 3988.
- (19) Dresselhaus, M. S.; Dresselhaus, G.; Eklund, P. C. *Science of Fullerenes and Carbon Nanotubes*; Academic Press: New York, 1996; Chapter 19.
- (20) Kiang, C. H.; Goddard, W. A.; Beyers, R.; Bethune, D. S. *Carbon* **1995**, 33, 903.
- (21) Dai, H. In *Carbon Nanotubes. Synthesis, Structure, Properties, and Applications*; Dresselhaus, M. S., Dresselhaus, G., Avouris, Ph., Eds.; Springer: Berlin, 2001; p 29.

- (22) Ajayan, P. M.; Zhou, O. Z. In *Carbon Nanotubes. Synthesis, Structure, Properties, and Applications*; Dresselhaus, M. S., Dresselhaus, G., Avouris, Ph., Eds.; Springer: Berlin, 2001; p 391.
- (23) Calbi, M. M.; Gatica, S. M.; Bojan, M. J.; Cole, M. W. *J. Chem. Phys.* **2001**, *115*, 9975.
- (24) Calbi, M. M.; Cole, M. W.; Gatica, S. M.; Bojan, M. J.; Stan, G. *Rev. Mod. Phys.* **2001**, *73*, 857.
- (25) Zambano, A. J.; Talapatra, S.; Migone, A. D. *Phys. Rev. B* **2001**, *64*, 075415-1.
- (26) Muris, M.; Dufau, N.; Bienfait, M.; Dupont-Pavlovsky, N.; Grillet, Y.; Palmari, J. P. *Langmuir* **2000**, *16*, 7019.
- (27) Muris, M.; Dupont-Pavlovsky, N.; Bienfait, M.; Zeppenfeld, P. *Surf. Sci.* **2001**, *492*, 67.
- (28) Yin, Y. F.; Mays, T.; McEnaney, B. *Langmuir* **1999**, *15*, 8714.
- (29) Wang, Q.; Johnson, J. K. *J. Chem. Phys.* **1999**, *110*, 577.
- (30) Mackie, E. B.; Wolfson, R. A.; Arnold, L. M.; Lafi, K.; Migone, A. D. *Langmuir* **1997**, *13*, 7197.
- (31) Du, W. F.; Ripmeester, J.; Dutrisac, R.; Simard, B.; Dénommée, S. *Nano Lett.* **2002**, *2*, 342.
- (32) Zhao, J.; Buldum, A.; Han, J.; Lu, J. P. *Nanotechnology* **2002**, *13*, 195.
- (33) Alain, E.; Yin, Y. F.; Mays, T. J.; McEnaney, B. *Stud. Surf. Sci. Catal.* **2000**, *128*, 313.
- (34) Fujiwara, A.; Ishii, K.; Suematsu, H.; Kataura, H.; Maniwa, Y.; Suzuki, S.; Achiba, Y. *Chem. Phys. Lett.* **2001**, *336*, 205.
- (35) Murata, K.; Kaneko, K.; Steele, W. A.; Kokai, F.; Takahashi, K.; Kasuya, D.; Hirahara, K.; Ydasaka, M.; Iijima, S. *J. Phys. Chem. B* **2001**, *105*, 10210.
- (36) Yanagi, H.; Sawada, E.; Manivannan, A.; Nagahara, L. A. *Appl. Phys. Lett.* **2001**, *78*, 1355.
- (37) Hassanien, A.; Mrzel, A.; Tokumoto, M.; Tománek, D. *Appl. Phys. Lett.* **2001**, *79*, 4210.
- (38) Martínez-Alonso, A.; Tascón, J. M. D.; Bottani, E. J. *J. Phys. Chem. B* **2001**, *105*, 135 and references herein.
- (39) Bottani, E. J.; Bakaev, V. A. *Langmuir* **1994**, *10*, 1550.
- (40) Bandow, S.; Asaka, S.; Saito, Y.; Rao, A. M.; Grigorian, L.; Richter, E.; Eklund, P. C. *Phys. Rev. Lett.* **1998**, *80*, 3779.
- (41) Méténier, K.; Bonnamy, S.; Béguin, F.; Journet, C.; Bernier, P.; Lamy de la Chapelle, M.; Chauvet, O.; Lefrant, S. *Carbon* **2002**, *40*, 1765.
- (42) Chattopadhyay, D.; Galeska, I.; Papadimitrakopoulos, F. *Carbon* **2002**, *40*, 985.
- (43) Bourguin, A.; Dupont-Pavlovsky, N. A.; Naji, A.; Ghanbaja, J.; Maréché, J. F.; Billaud, D. *Carbon* **2001**, *39*, 685.
- (44) Paredes, J. I.; Martínez-Alonso, A.; Tascón, J. M. D. *Langmuir* **2002**, *18*, 4314.
- (45) Chen, Y.; Haddon, R. C.; Fang, S.; Rao, A. M.; Eklund, P. C.; Lee, W. H.; Dickey, E. C.; Grulke, E. A.; Pendergrass, J. C.; Chavan, A.; Haley, B. E.; Smalley, R. E. *J. Mater. Res.* **1998**, *13*, 2423.
- (46) Monthieux, M.; Smith, B. W.; Burteaux, B.; Clayer, A.; Fischer, J. E.; Luzzi, D. E. *Carbon* **2001**, *39*, 1251.
- (47) Paredes, J. I.; Martínez-Alonso, A.; Tascón, J. M. D. *Langmuir* **2001**, *17*, 474.
- (48) Kaneko, K. *Carbon* **2000**, *38*, 287.
- (49) Bojan, M. J.; Vernov, A. V.; Steele, W. A. *Langmuir* **1992**, *8*, 901.
- (50) Ohba, T.; Kaneko, K. *J. Phys. Chem. B* **2002**, *106*, 7171.
- (51) Cascarini de Torre, L. E.; Bottani, E. J. *An. Quím.* **1995**, *91*, 334.